Interfacial Molecular Compatibility for Programming Organic−Metal Oxide Superlattices

Takeshi Ono, Sae Mitamura, Takuro Hosomi,* Hikaru Saito, Midori Ikeuchi, Jiangyang Liu, Kazuki Nagashima, Tsunaki Takahashi, Wataru Tanaka, Masaki Kanai, and Takeshi Yanagida*

Cite This: ACS Appl. Mater. Interfaces 2023, 15, 27099−27109   Read Online

ACCESS | Metrics & More | Article Recommendations | Supporting Information

ABSTRACT: Artificially programming a sequence of organic−metal oxide multi-layers (superlattices) by using atomic layer deposition (ALD) is a fascinating and challenging issue in material chemistry. However, the complex chemical reactions between ALD precursors and organic layer surfaces have limited their applications for various material combinations. Here, we demonstrate the impact of interfacial molecular compatibility on the formation of organic−metal oxide superlattices using ALD. The effects of both organic and inorganic compositions on the metal oxide layer formation processes onto self-assembled monolayers (SAM) were examined by using scanning transmission electron microscopy, in situ quartz crystal microbalance measurements, and Fourier-transformed infrared spectroscopy. These series of experiments reveal that the terminal group of organic SAM molecules must satisfy two conflicting requirements, the first of which is to promptly react with ALD precursors and the second is not to bind strongly to the bottom metal oxide layers to avoid undesired SAM conformations. OH-terminated phosphate aliphatic molecules, which we have synthesized, were identified as one of the best candidates for such a purpose. Molecular compatibility between metal oxide precursors and the −OHs must be properly considered to form superlattices. In addition, it is also important to form densely packed and all-trans-like SAMs to maximize the surface density of reactive −OHs on the SAMs. Based on these design strategies for organic−metal oxide superlattices, we have successfully fabricated various superlattices composed of metal oxides (Al-, Hf-, Mg-, Sn-, Ti-, and Zr oxides) and their multilayered structures.

KEYWORDS: superlattice, atomic layer deposition, self-assembled monolayer, organic−inorganic hybrid materials, metal oxide nanowires
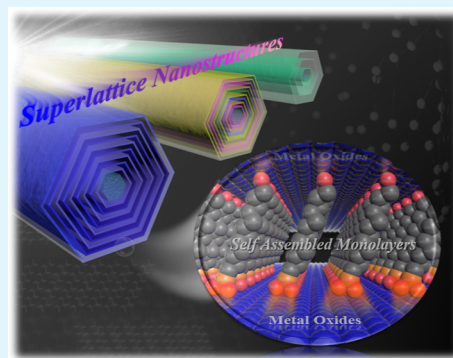
INTRODUCTION

Organic−metal oxide superlattices, which consist of alternating nano-layers of organic and metal oxide materials, have attracted much attention due to novel characteristics and functionalities via their rich material combinations.[1−4] Solution-phase synthetic methods are typically used to yield a large amount of organic−metal oxide superlattices under relatively mild conditions.[5−9] However, it is essentially difficult for such bulk synthetic methods to precisely manipulate the orientation and thickness of each layer of the superlattices. In order to overcome the above issues, new fabrication methods that utilize atomic layer deposition (ALD)[10−14] have been recently developed.[15−19] First, organic self-assembled mono-layers (SAM) are formed by supplying the molecules via vapor or solution phases and then organometallic species and H_2O or O_3 are alternately supplied to form a metal oxide layer, whose thickness can be precisely controlled by the cycle numbers. When compared with conventional ALD processes, this method is unique because it is intended that highly reactive organometallic species are reacted on the top of organic layers at high temperatures to form metal oxide layers. Although several examples have been successfully demonstrated,[1−4,15−17]

it is still difficult to arbitrarily tailor organic−metal oxide superlattices using ALD. This is mainly due to the lack of comprehensive studies of ALD processes on organic molecules.[3,20−25] One of the major reasons for this is the difficulty to perform morphological analysis [e.g., transmission electron microscopy (TEM)[26,27], spectroscopic reaction tracking [e.g., Fourier-transformed infrared spectroscopy (FT-IR)[28,29]], and quantitative deposition monitoring [e.g., quartz crystal microbalance (QCM)[30−33]] on the identical sample. Recently, we developed single-crystal oxide nanowires as a comprehensive platform for these analyses.[34−36] The arrays of the single-crystal nanowires are suitable for FT-IR and QCM because their large surface area can significantly amplify signals obtained from small amounts of monolayer com-pounds. At the same time, each nanowire has flat single-crystal
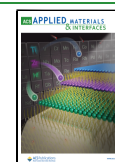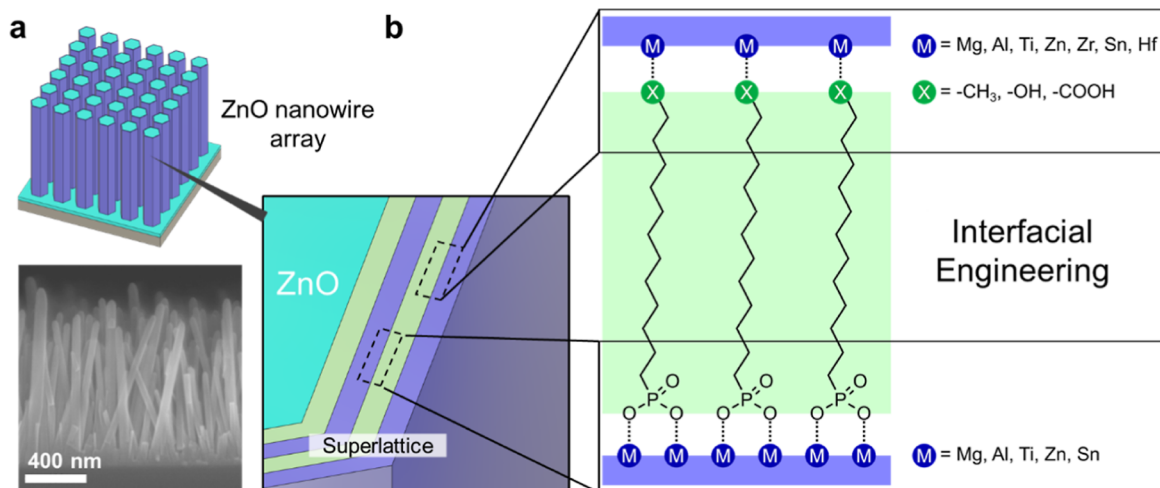
Figure 1. Concept of interfacial engineering in this work. (a) Illustrated structure and a SEM image of the ZnO nanowire array used as the platform of the superlattice. (b) Schematic image of a superlattice. An aliphatic SAM (middle layer) is fabricated on a metal oxide layer (bottom layer), and another metal oxide layer (top layer) is deposited on the SAM. The interfaces between bottom and middle layers or top and middle layers are examined in this work.
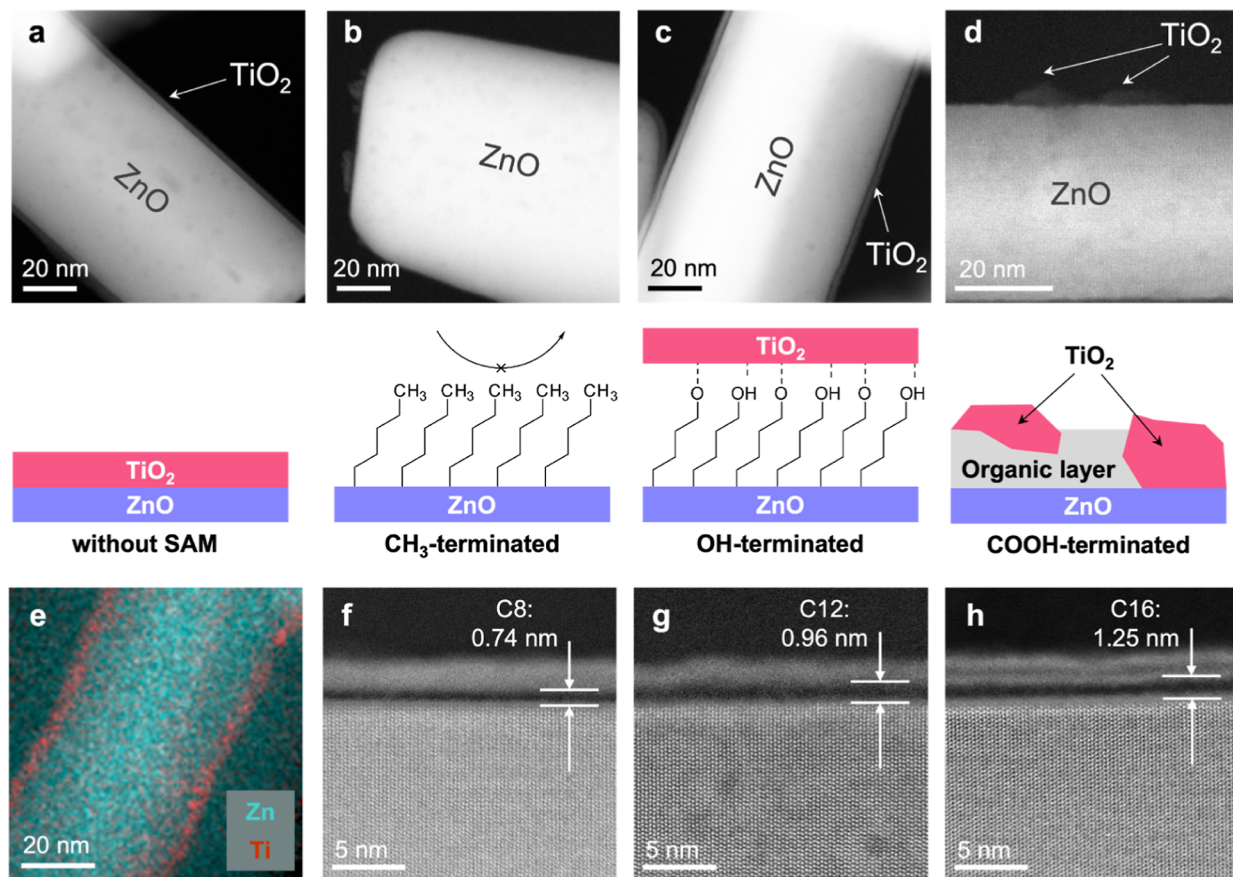

Figure 2. STEM images ZnO nanowires after 40-cycle ALD depositions of TiO_2 on (a) a bare ZnO nanowire, (b) CH_3-terminated SAM on a ZnO nanowire, (c) OH-terminated SAM on a ZnO nanowire, and (d) COOH-terminated SAM on a ZnO nanowire. The EDS elemental mapping image of (c) is shown in (e). Magnified STEM images of TiO_2 layers on OH-terminated SAMs with varying alkyl chain lengths of 8, 12, and 16 are shown in (f–h). Each of the thickness values was obtained by taking 13 points of the distance between the bottom and top metal oxide layers and averaging them.

facets with well-defined edges, making it possible to observe precisely aligned cross-sections by scanning TEM (STEM) without complex destructive procedures including etching and milling.

In this study, organic–metal oxide superlattices consisting of (1) bottom metal oxide layers, (2) intermediate organic SAMs, and (3) top metal oxide layers were formed on ZnO nanowires (Figure 1). Various elements (Zn, Mg, Al, Ti, Sn, Zr, and Hf)
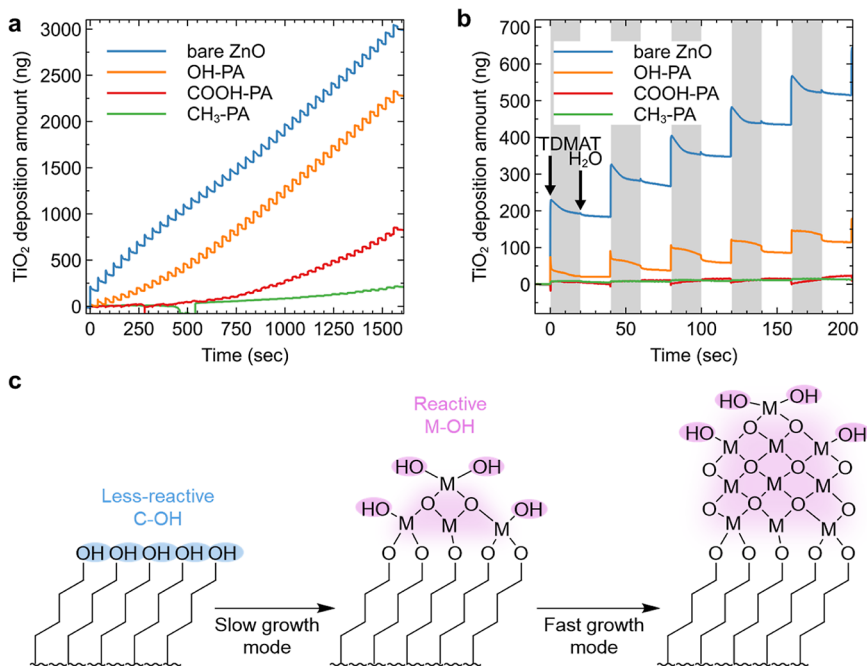
Figure 3. (a) Mass gain data during ALD of TiO$_2$ on SAM-modified or unmodified (bare) ZnO nanowires obtained by in situ QCM. (b) Magnified mass gain data during the first five cycles of ALD, where tetrakis(dimethylamino)titanium (Ti(NMe$_2$)$_4$, TDMAT) and H$_2$O were introduced alternately. (c) Schematic image of the early slow growth mode and later fast growth mode of ALD on OH-terminated SAMs.

were examined as the top and bottom metal oxide layers. Alkyl phosphonic acids, which are known to bind stably on a wide range of metal oxides,[37−43] were used as the intermediate SAMs, and their length and terminal functional groups were investigated. The superlattice formation process in these various combinations was analyzed by STEM morphology analyses, FT-IR chemical reaction tracings, and QCM deposition monitoring to evaluate the effects of each layer structure on the ALD on SAMs.

■ RESULTS AND DISCUSSION

First, we investigate the effects of the functional groups (−CH$_3$, −OH, and −COOH) of SAMs on the metal oxide layer formation using ALD, as illustrated in Figure 1. TiO$_2$ depositions using tetrakis(dimethylamino)titanium (Ti-(NMe$_2$)$_4$, TDMAT) and H$_2$O were performed onto ZnO nanowire surfaces (bare ZnO) and nanowire surfaces decorated by three kinds of aliphatic phosphonic acids: dodecylphosphonic acid (CH$_3$-PA), (12-hydroxydodecyl)-phosphonic acid (OH-PA), and 12-phosphonododecanoic acid (COOH-PA). The synthetic procedures of these molecules can be seen in the Experiment section. These ZnO nanowires were hydrothermally grown onto the c-axis-oriented ZnO seed layer prepared by rf-sputtering, as reported elsewhere.[44−46] Note that Si substrates were used for microstructural analysis using microscopy and spectroscopic characterizations using IR, and quartz substrates with Au electrodes were employed for QCM experiments, which allowed us to monitor in situ mass gain data during the ALD process. We confirmed that the quality of fabricated ZnO nanowire surfaces is not affected by the substrate types due to the uniformity of fabricated ZnO seed layer crystallinity (Figure S1). This enables us to comprehensively analyze nearly identical samples by three different methods-STEM, IR, and in situ QCM.

Figure 2 shows the effects of different ZnO surface decorations on microstructural data of STEM images for ALD-grown TiO$_2$ nanostructures. The ALD cycle number was set to be 40 unless otherwise indicated. It is noted that all the observed nanowire orientations were adjusted so that the electron beam was parallel to 11−20, i.e., the projection direction was always parallel to, the atomically flat m-plane of ZnO surfaces to precisely visualize the cross-sectional ALD layer morphology and thickness. As clearly seen in Figure 2a−d, there is a distinct discrepancy between different surface decorations on the morphology of TiO$_2$ nanostructures. In particular, the effect of SAM's terminal group is significant. In the case of the OH-SAM (Figure 2c), there is a spatially uniform ZnO-SAM-TiO$_2$ layer-by-layer (superlattice) structure. The energy-dispersive X-ray spectroscopy (EDS) elemental mapping image in Figure 2e also supports the floating TiO$_2$ nanostructures onto SAMs. Such spatially uniform TiO$_2$ deposition is also found on bare ZnO nanowire surfaces, as seen in Figure 2a. The TiO$_2$ on the OH-SAM is slightly thinner than that on the bare ZnO. On the other hand, there are almost no TiO$_2$ depositions on CH$_3$-SAM (Figure 2b) and fewer depositions on COOH-SAM (Figure 2d) decorated surfaces. Thus, it is possible to deposit TiO$_2$ nanostructures onto SAMs using ALD by appropriately selecting the terminal group. The estimated organic layer thickness is measured to be 0.96 nm for the OH-SAM (C12) from STEM images, which is consistent with the estimated value of inclined SAM height (Figure S2 and Table S1). The organic layer thickness of superlattice structures can be arbitrarily controlled by varying the SAM's chain length (Figure 2f−h). We have synthesized these different carbon number molecules-OH-SAM (C8, C12, and C16), as described in the section of Experiment. It can be seen from Figure 2f−h that the lengths observed as organic layers were 0.74 and 1.25 nm for C8 SAM and C16 SAM, respectively. These values are also consistent with the estimated values of
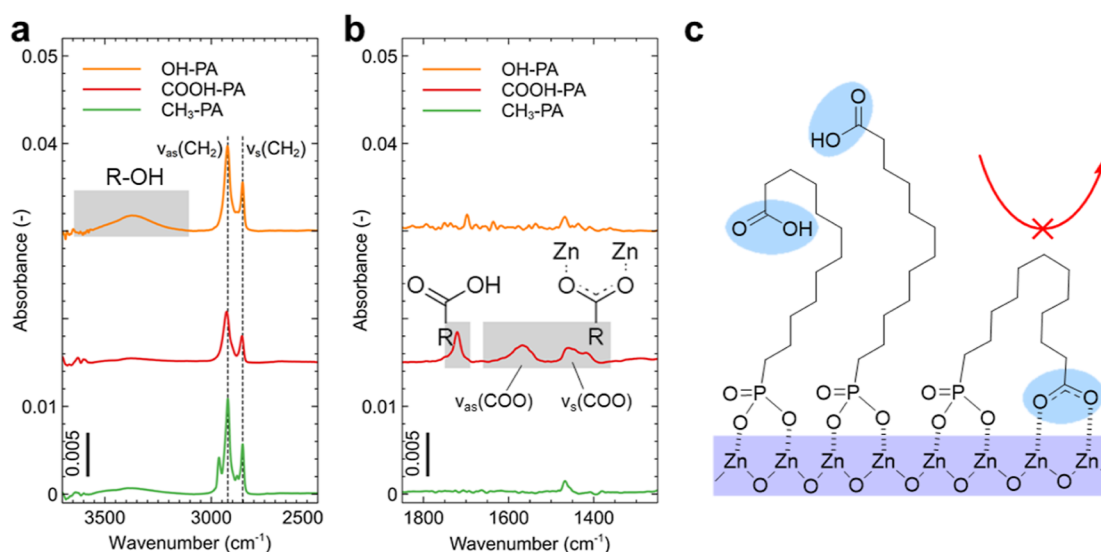
Figure 4. FT-IR spectra of OH-PA (yellow), COOH-PA (red), and CH$_3$-PA (green) in the (a) alkyl regions and (b) carbonyl region. ν_{as}(CH$_2$) and ν_s(CH$_2$) are the asymmetric and symmetric vibration mode of CH$_2$, respectively. ν_{as}(COO) and ν_s(COO) are the asymmetric and symmetric vibration mode of the carboxylate, respectively. (c) Schematic image to explain the low-reactivity of COOH-SAM on ZnO with ALD precursors.

inclined SAM heights (Table S1). These consistencies between superlattice structures and molecular lengths further support the existence of ZnO-SAM-TiO$_2$ superlattice structure. Thus, these results reveal the critical role of terminal groups of SAMs on the formation of ZnO-SAM-TiO$_2$ superlattice structures by ALD, highlighting the superior characteristics of OH-PA SAM as the ALD platform. Although the absence of superlattice structures for CH$_3$-SAM in Figure 2b is a straightforward result by considering the fundamental principle of ALD processes,[10,11,21] the result for COOH-SAM is inconsistent with the conventional trend of ALD chemical reactions, which explains the −COOH group as an appropriate reactive group for ALD processes.[20,47,48]

To further examine the effect of terminal groups of SAMs on the formation process of ZnO-SAM-TiO$_2$ superlattice structures, we have performed in situ QCM experiments during the ALD processes to monitor the mass gain data. Figure 3a,b shows the effects of terminal groups on the mass gain data. These samples' surface modifications are identically performed as those in Figure 2. As clearly seen, there are significant differences between different terminal groups of SAMs on mass gain data, which are almost consistent with the experimental trends of STEM images in Figure 2. There is reasonable mass gain data for bare ZnO and OH-SAM samples, and no significant mass gain data for CH$_3$-SAM and COOH-SAM samples. The intensity order of mass gain data is bare-ZnO > OH-SAM > COOH-SAM > CH$_3$-SAM. The QCM mass gain data of the bare ZnO show periodic mass changes synchronizing with the QCM cycles (Figure 3a,b, blue line). There is a sharp mass gain pulse at the moment of TDMAT introduction, followed by a monotonous decrease except for a slight change at the moment of H$_2$O introduction. This is known to be a typical QCM behavior of a successful ALD process.[49,50] On the other hand, CH$_3$-SAM does not show any mass gains during the ALD process (Figure 3a,b, green line). This trend indicates that CH$_3$-SAM has a high blocking ability against TDMAT access to the ZnO surface as previously studied.[51−53] In contrast, OH-PA SAM shows a clear periodic mass gain pattern (Figure 3a,b, yellow line) as observed in the bare ZnO. Thus, the terminal hydroxyl groups

effectively act as the initial point of the ALD process. When comparing OH-PA SAM and bare ZnO data, there are several features of these mass gain data. First, at the initial ALD cycle stages around below 15 cycles (500−600 s), the growth rate of OH-PA SAM is significantly lower than bare ZnO data. At later ALD cycle stages above 15 cycles, both the growth rates of OH-PA SAM and bare ZnO data are almost identical. Thus, the overall QCM mass gain data of the OH-PA SAM can be divided into two stages: the early slow growth mode and the later fast growth mode (Figure 3c). This behavior can be interpreted in terms of the reactivity differences between carbon−OH and metal−OH. Since the carbon−OHs are less reactive to TDMAT than metal−OH possibly due to their different circumstances of molecular reactions (including their surface density and reactivity), the growth rate of the early stage is much slower. As TiO$_2$ deposition progresses, the surface hydroxyl groups tend to be dominated by metal−OH (Ti−OH), which accelerates the growth rate to the same level as bare ZnO. The deposition QCM mass gain data are fitted by a reported model to be classified into the early and later deposition modes.[32,54] The transition cycle (TC), at which the transition from the early slow growth mode to the later fast growth mode occurs, can be defined. The TC value of OH-SAM in Figure 3a is estimated to be 15 by using the above fitting model (Figure S3). Next, we focus on the mass gain data trend of COOH-SAM by comparing with others. The TiO$_2$ deposition on the COOH-SAM is much slower than that of the OH-SAM, and the behavior is rather similar to that of CH$_3$-SAM (Figure 3a,b, red line). In fact, these trends are consistent with the microstructural data of STEM images in Figure 2. Since some previous studies suggest that the −COOH group is a good functional group for ALD depositions,[20,47,48] these experimental trends cannot be easily understood as long as we assume conventional SAM conformations with −COOH functional group at the top of the layer and −PA head group attached onto ZnO surface. It is inferred that for some structural reasons of COOH-SAM on ZnO, −COOH is less likely to act as an ALD initiation site.

To answer the abovementioned question on COOH-SAM data, we measure the molecular conformations of SAMs on
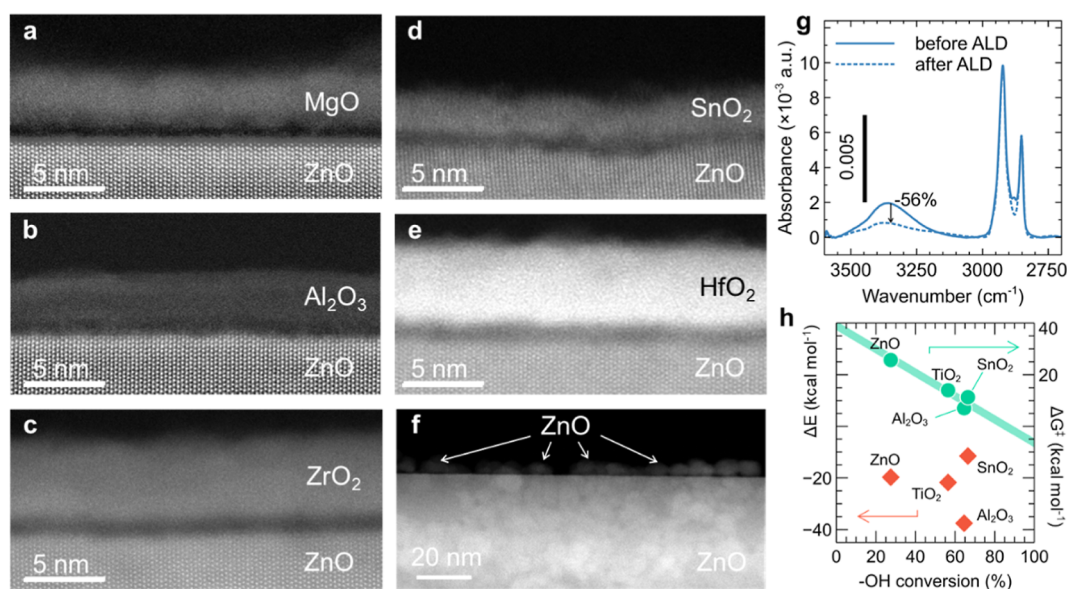
Figure 5. Magnified STEM images of ALD-deposited nanostructures of (a) MgO, (b) Al$_2$O$_3$, (c) ZrO$_2$, (d) SnO$_2$, and (e) HfO$_2$ on OH-terminated SAMs modified on nanowires. The STEM image of ZnO (f) shows that the deposition is not uniform, resulting in a sparse particulate deposition. (g) FT-IR spectra before (solid line) and after (hashed line) TiO$_2$ ALDs. (h) Calculated reaction enthalpy (ΔE) and activation energy ($\Delta G^{\ddagger}$) of reactions between −OH and each metal oxide precursor plotted against OH conversion calculated by FT-IR. Details of the calculation are shown in Figures S7 and S8.

ZnO surfaces by using infrared spectroscopy. Figure 4a,b show the comparison between different terminal groups (−OH, −COOH, and −CH$_3$) of SAMs on FT-IR spectra. The two major peaks in the region of 2800−3000 cm^{-1} can be assigned to methylene symmetric $[\nu_s(CH_2)]$ and asymmetric $[\nu_{as}(CH_2)]$ stretching vibrations. Wavenumbers of $\nu_s(CH_2)$ and $\nu_{as}(CH_2)$ reflect the trans and cis conformational occupancy, which can be used as indicators of SAM packing degree. The greater the degree of packing, the smaller the wavenumber values.[55−57] The wavenumbers of $\nu_s(CH_2)$ = 2852.35 cm^{-1} and $\nu_{as}(CH_2)$ = 2922.35 cm^{-1} observed in the SAM of dodecylphosphonic acid (CH$_3$-PA) are consistent with the literature, which indicates a dense packing of the SAM.[58] The SAM of OH-terminated phosphonic acid (OH-PA) shows slightly higher $\nu_s(CH_2)$ and $\nu_{as}(CH_2)$ wavenumbers (2852.77 and 2923.71 cm^{-1}), which indicates the disordered packing of the OH-SAM, as discussed in the previous works.[59] In contrast to the two abovementioned SAMs, the methylene stretching vibrations of the COOH-SAM exhibit significantly higher wavenumbers ($\nu_s(CH_2)$ = 2855.84 cm^{-1}, $\nu_{as}(CH_2)$ = 2928.11 cm^{-1}) and lower peak intensities. These results reveal that the COOH-SAM is sparser and more disordered when compared with typical SAMs. In addition, typical symmetric and asymmetric carboxylate peaks placed around 1460 and 1570 cm^{-1} are observed in Figure 4b,[60] clearly indicating that many −COOH groups are not pointing upward but are bonded to the ZnO surface, forming possibly a U-shaped bent structure. Thus, these spectroscopic data well explain the absence of ALD crystal growths on COOH-SAM surfaces in terms of such U-shaped SAM conformations with less −COOH on the top of the SAM (Figure 4c). The underlying mechanism to form such U-shaped SAM conformations is the inevitable strong reactivity between −COOH groups of SAMs and metal oxide surfaces during SAM formation processes. From the viewpoint of this implication, OH-SAM, which we have synthesized, is one of the best candidates to form organic−metal oxide superlattices by using ALD processes.

Here, we investigate the applicability of OH-SAMs on the formations of various organic−metal oxide superlattices by using various metal oxides (MgO, Al$_2$O$_3$, TiO$_2$, ZnO, ZrO$_2$, SnO$_2$, or HfO$_2$). Figure 5a−e shows the cross-sectional STEM images of the metal oxide layers deposited onto OH-SAMs. It can be seen that MgO, Al$_2$O$_3$, ZrO$_2$, SnO$_2$, and HfO$_2$ layers were successfully deposited onto the SAMs with the spatial uniformity. However, ZnO shows a heterogeneous grain-like deposition onto the SAM, as seen in Figure 5f. To understand this difference between metal oxides on the superlattice formations, we consider the reactivity (compatibility) between ALD metal oxide precursors and −OH groups of SAM. As shown in Figure 5g of FT-IR spectra for TiO$_2$ ALD, the intensity of the −OH peak at 3380 cm^{-1} decreases after the ALD, corresponding to the conversion from the terminal −O−H to the −O−M structure. By measuring the IR peak intensity differences during ALD processes, it is possible to quantify the degree of conversion progress. Metal oxides (MgO, Al$_2$O$_3$, ZrO$_2$, SnO$_2$, and HfO$_2$), which exhibited successful superlattice structures in Figure 5a−e, show significant reductions of the −OH peaks (Figure S7). In contrast, these decreases are much lower in the case of the ZnO ALD (Figure S7). These differences in reactivities of metal oxide species can be attributed to the activation energies of the reactions between their precursors and the OH-SAM. The calculated activation energies of the reactions with simplified models show linear relationships with the −OH conversions, whereas their calculated reaction enthalpies do not have such clear correlations (Figure 5h).[20,61] Thus, these results highlight that OH-SAM has good compatibility with various metal oxide precursors for ALD processes, and it is also important to select a metal oxide precursor, which has a low activation energy for the reaction with the alcoholic OH group of SAMs.

Next, we examine the applicability of OH-PA SAMs when varying metal oxide bottom layers as a scaffold for the SAMs. TiO$_2$ ALDs were performed on OH-SAMs on the four metal oxide bottom layers (ZnO, Al$_2$O$_3$, TiO$_2$, and SnO$_2$), and the
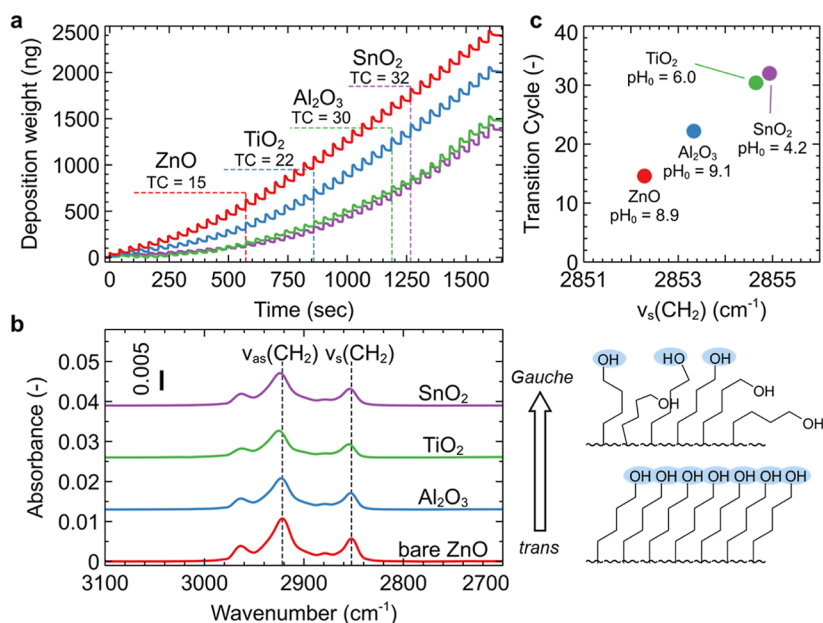
Figure 6. (a) Mass gain data during TiO_2 ALD onto OH-terminated SAMs modified on various metals (red: bare ZnO, blue: TiO_2, green: Al_2O_3, and purple: SnO_2) observed by in situ QCMs. (b) FT-IR spectra of OH-terminated SAMs modified on various metals (red: bare ZnO, blue: TiO_2, green: Al_2O_3, and purple: SnO_2) to evaluate the conformational enrichments of their alkyl chains. (c) TCs of QCM mass gain data plotted against $\nu_s(CH_2)$ peak wavenumber for each bottom layer compound. The values of pH_0 are the zero charge points of each metal oxide.
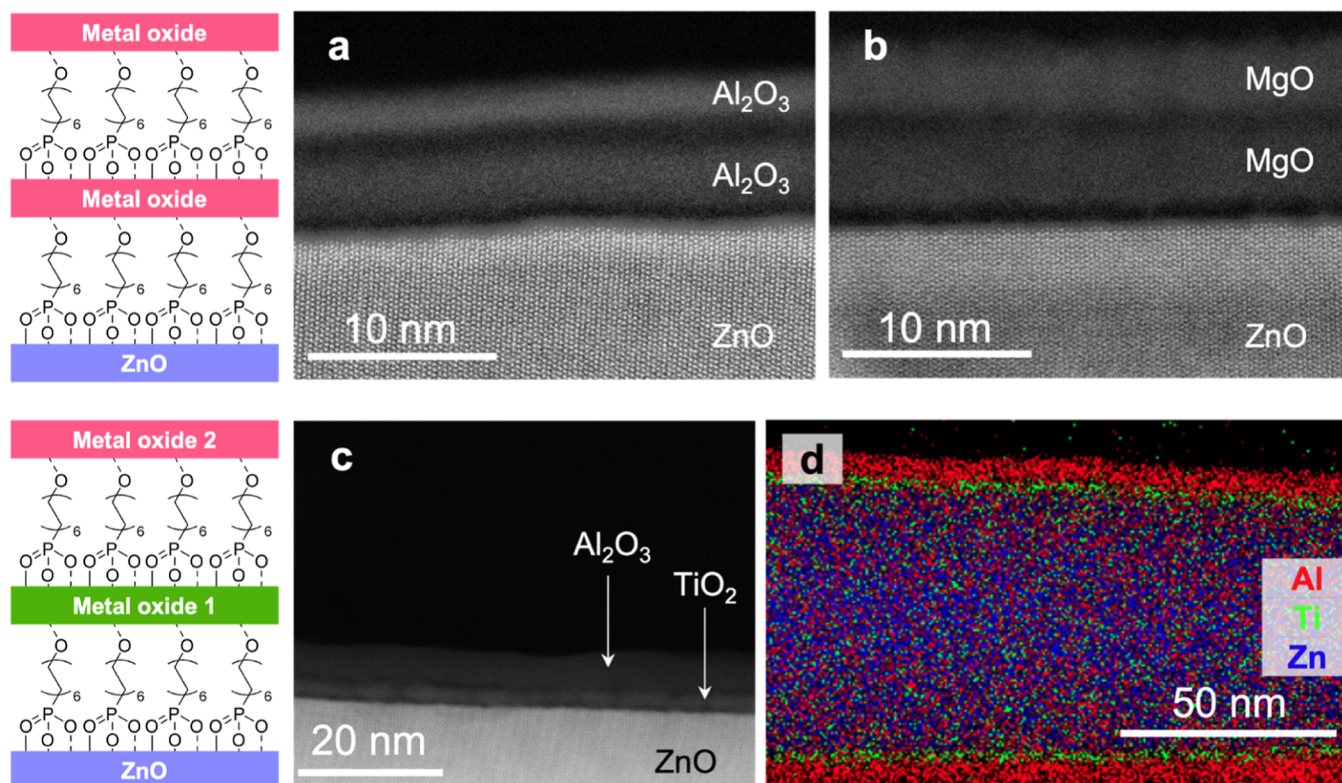

Figure 7. STEM images of double-layered organic–inorganic superlattices fabricated on ZnO nanowires with OH-PA and metal oxides. Composition of layers are (a) first: Al_2O_3, second: Al_2O_3, (b) first: MgO, second: MgO, and (c) first: TiO_2, second: Al_2O_3 (80 cycles). The EDS elemental mapping image (red: Al, green: Ti, and blue: Zn) of the sample (c) is shown in (d).

amounts of depositions were monitored by QCM (Figure 6a). Periodic mass increase profile is consistently observed in all samples, although there are differences in their deposition rate profiles, especially in the early ALD cycle stage. By using fitted parameters (TC) as discussed in Figures 3 and S3, we can

evaluate the reactivity of ALD precursor-TDMAT to OH-SAM immobilized on the different metal oxides. The order of reactivities with TDMAT is estimated to be SAM on ZnO (TC = 15) > SAM on Al_2O_3 (TC = 22) > SAM on TiO_2 (TC = 30) > SAM on SnO_2 (TC = 32). Since the SAM molecular

structure itself is common for these ALD depositions, the reactivity discrepancy might be attributed to the different molecular conformations of the SAMs on the different metal oxide surfaces. Figure 6b shows the FT-IR spectra of OH-SAMs modified on four different metal oxides. It can be seen that the peak wavenumbers of $\nu_s(CH_2)$ and $\nu_{as}(CH_2)$ are larger for ZnO, Al_2O_3, TiO_2, and SnO_2, in that order. Since the larger wavenumbers more disordered SAM structures with larger proportions of Gauche conformation, the order of the degree of molecular disorderness is $SnO_2 > TiO_2 > Al_2O_3 > ZnO$, as illustrated in the figure. Similar trends are also observed when the terminal functional groups are CH_3 (Figure S9). Interestingly, as shown in Figure 6c, the order of molecular disorderness [the wavenumber of $\nu_s(CH_2)$] is consistent with that of TC values, indicating that the TC number from the initial slow growth mode (metal oxide deposition on −carbon−OH) to the later fast growth mode (metal oxide deposition on −metal−OH) is determined by the molecular conformation of SAMs. This is because less ordered SAMs are considered to cause lower densities of reactive OH exposed on the surface, which result in lower ALD reaction rates. Furthermore, the $\nu_s(CH_2)$ and $\nu_{as}(CH_2)$ peak wavenumbers of the OH-SAM well correlate with the zero charge point (pH_0) of the metal oxides, as shown in Figure 6c. The values of pH_0 are from the literature.[62] This trend can be explained by stronger interactions of more basic metal oxides with phosphonic acids of SAMs. These results highlight the important role of interfacial compatibility between a head group of SAMs and a bottom metal oxide layer on superlattice formations using ALD. Finally, we examine the applicability of the present strategy using OH-SAMs for forming multilayered and hetero-superlattices, as shown in Figure 7. Figure 7a,b shows the STEM images of fabricated multilayered superlattices composed of ZnO-SAM-Al_2O_3-SAM-Al_2O_3 and ZnO-SAM-MgO-SAM-MgO, respectively. Clearly, the well-defined multilayered superlattice structures are observed for both cases. In the case of Al_2O_3 multilayered superlattices, the outer second Al_2O_3 layer is found to be slightly thinner than the inner first layer. This is because the conformation of the second SAM was identified to be more disordered Gauche-rich, resulting in the higher TC value as explained in Figure 6. More detailed information can be seen in Figure S10. Figure 7c shows the STEM images of fabricated ZnO-SAM-TiO_2-SAM-Al_2O_3, highlighting the applicability of the present method for various material combinations. The EDS elemental mapping image clearly shows that the superlattice structures were accumulated in the intended order (Figure 7d). Although we demonstrate several material combinations and applications of our method using OH-SAMs, the present strategy can be a useful guideline to arbitrarily program organic−inorganic superlattices.

CONCLUSIONS

We have demonstrated the impact of interfacial molecular compatibility on the formation of organic−metal oxide superlattices using ALD. The series of experiments reveal that the terminal group of organic SAM molecules must satisfy two conflicting requirements, the first of which is to promptly react with ALD precursors and the second is not to bind strongly to the bottom metal oxide layers to avoid undesired SAM conformations. OH-terminated phosphate aliphatic molecules, which we have synthesized, were identified as one of the best candidates for such a purpose. Molecular

compatibility between metal oxide precursors and the -OHs must be properly considered to form superlattices. In addition, it is also important to form densely packed and all-trans-like SAMs to maximize the number of reactive −OHs on the SAMs. Based on these design strategies for organic−metal oxide superlattices, we have successfully fabricated various superlattices composed of metal oxides (Al-, Hf-, Mg-, Sn-, Ti-, and Zr oxides) and their multilayered structures. The following three conditions are important for ALD on phosphonic acid SAMs on metal oxides. (1) The terminal functional group of the SAM must have low interaction with the bottom metal oxide while ensuring reactivity with the ALD precursor (e.g., −OH). (2) The deposited metal oxide species on the SAM must have a low activation energy for reaction with the SAM terminal functional group. (3) The bottom metal oxide must be highly basic to enable the formation of dense, ordered SAMs on top of it. To the best of our knowledge, this is the first example to fabricate nano-level organic−inorganic multi-layer structures using alternating solution-phase SAM formation and metal oxide ALD.

EXPERIMENT

Reagents. Zinc nitrate hexahydrate ($Zn(NO_3)_2 \cdot 6H_2O$, JIS-GR), hexamethylenetetramine (HMTA, JIS-GR), acetone (JIS-GR), methanol (JIS-GR, MeOH), CH_2Cl_2 (super dehydrated), $CHCl_3$ (JIS-GR), tetrahydrofuran (super dehydrated, THF), and 16-bromo-1-hexadecanol (JIS-GR) were purchased from FUJIFILM Wako Pure Chemical Corp. NaI (JIS-GR) and trimethylbromosilane (JIS-GR), dodecylphosphonic acid (JIS-GR), 8-bromo-1-octanol (JIS-GR), and 12-bromo-1-dodecanol (JIS-GR) were purchased from Tokyo Chemical Industry Co., Ltd. Polyethyleneimine (PEI, M_n = 1800, 50 wt % in H_2O) was purchased from Sigma-Aldrich Co. LLC. These reagents were used without further purification.

Growth of ZnO Nanowires. ZnO nanowire arrays on Si(100) wafers or QCM sensors were grown using the hydrothermal method.[63] First, a 1.5 nm Ti buffer layer was sputtered onto the substrate, and then a 45 nm ZnO film was sputtered on as the seed layer. 2.5 mM PEI, 25 mM HMTA, and 25 mM $Zn(NO_3)_2 \cdot 6H_2O$ were dissolved sequentially in distilled water (150 mL). The pre-prepared substrate was dipped into the solution and maintained at 95 °C for 6 h. After growth, the samples were rinsed with distilled water. Then the as-grown ZnO nanowires were annealed at 400 °C in the air for 30 min.

Synthesis of 2-(12-Bromododecyloxy)tetrahydro-2H-pyran (1). 1 was synthesized from 12-bromo-1-dodecanol according to the modified literature procedure.[64]

Synthesis of 2-(12-Iodododecyloxy)tetrahydro-2H-pyran (2). To a solution of NaI (1.00 g, 6.67 mmol) in acetone (10 mL) was added 1 (1.14 g, 3.26 mmol). The reaction was stirred at room temperature for 12 h, after which the white solid of NaBr was removed by filtration. The mixture was concentrated and a white solid of excess NaI was filtered to afford a yellow oil 2 (1.26 g, 98%). ^1H NMR (400 MHz, $CDCl_3$): δ = 4.57 (dd, J = 4.4, 2.7 Hz, 1H), 3.86 (d, J = 11.1 Hz, 1H), 3.73 (dt, J = 9.6, 6.9 Hz, 1H), 3.51−3.50 (m, 1H), 3.38 (dt, J = 9.6, 6.7 Hz, 1H), 3.19 (t, J = 7.1 Hz, 2H), 1.85−1.57 (m, 9H), and 1.40−1.25 (m, 17H).

Synthesis of Diethyl 12-[(2-Tetrahydro-2H-pyranyl)-oxy]dodecyl-phosphonate (3). 3 was synthesized from 2 according to the modified literature procedure.[64] Crude 3 was used for the next reaction without further purification.

Synthesis of (12-Hydroxydodecyl)phosphonic Acid (OH-PA, 4). 4 was synthesized from 3 according to the modified literature procedure[64] as follows. To a solution of 3 (0.894 g, 2.20 mmol) in dry CH_2Cl_2 (30 mL) was added trimethylbromosilane (3 mL, 21.6 mmol). The mixture was stirred under Ar at room temperature for 24 h, and then MeOH (30 mL) was added and stirred for 24 h. The mixture was then concentrated and recrystallized with acetone to afford a white solid 4 (0.116 g, 20%). ^{1}H NMR (400 MHz, CD_3OD): δ = 3.54 (t, J = 6.6 Hz, 2H), 1.70−1.30 (m, 22H).

Synthesis of 2-(16-Bromohexadecyloxy)tetrahydro-2H-pyran (5). 5 was synthesized from 16-bromo-1-hexadecanol according to the modified literature procedure.[64]

Synthesis of 2-(16-Iodohexadecyloxy)tetrahydro-2H-pyran (6). To a solution of NaI (1.00 g, 6.67 mmol) in acetone (10 mL) was added 5 (1.20 g, 2.96 mmol). The reaction was stirred at room temperature for 3 h, after which the white solid of NaBr was removed by filtration. The mixture was concentrated and a white solid of excess NaI was filtered to afford a yellow oil 6 (1.31 g, 98%). ^{1}H NMR (400 MHz, $CDCl_3$): δ = 4.57 (dd, J = 4.2, 2.8 Hz, 1H), 3.90−3.84 (m, 1H), 3.73 (dt, J = 9.6, 6.9 Hz, 1H), 3.53−3.47 (m, 1H), 3.38 (dt, J = 9.5, 6.7 Hz, 1H), 3.19 (t, J = 7.1 Hz, 2H), 1.86−1.78 (m, 3H), 1.75−1.68 (m, 1H), 1.62−1.58 (m, 2H), 1.55−1.49 (m, 3H), and 1.42−1.27 (m, 25H).

Synthesis of 16-[(2-Tetrahydro-2H-pyranyl)oxy]-hexadecyl-phosphonate (7). 7 was synthesized from 6 according to the modified literature procedure.[64] Crude 7 was used for the next reaction without further purification.

Synthesis of (16-Hydroxydodecyl)phosphonic Acid (8). 8 was synthesized from 7 according to the modified literature procedure[64] as follows. To a solution of crude 7 (2 mmol) in dry CH_2Cl_2 (20 mL) was added trimethylbromosilane (3 mL, 21.6 mmol). The mixture was stirred under Ar at room temperature for 24 h, and then MeOH (20 mL) was added and stirred for 24 h. The mixture was then concentrated and recrystallized with acetone and ethanol to afford a white solid 8 (0.515 g, 80%). ^{1}H NMR (400 MHz, CD_3OD): δ = 3.56−3.51 (m, 2H), 1.72−1.38 (m, 30H).

Synthesis of (8-Hydroxyoctyl)phosphonic Acid (9). 9 was synthesized from 8-bromo-1-octanol according to the same procedure as for (12-hydroxydodecyl)phosphonic acid 4 and (16-hydroxyhexadecyl)phosphonic acid 8.

Synthesis of 12-Bromododecanoic Acid (10). 10 was synthesized from 12-bromo-1-dodecanol according to the literature procedure.[65]

Synthesis of Ethyl 12-(Diethoxyphosphoryl)-dodecanoate (11). 11 was synthesized from 10 according to the modified literature procedure.[66]

Synthesis of 12-Phosphonododecanoic Acid (COOH-PA, 12). To a solution of 11 (1.25 g, 3.44 mmol) in dry CH_2Cl_2 (30 mL) was added trimethylbromosilane (3 mL, 21.6 mmol). The mixture was stirred at room temperature under Ar for 24 h, and then MeOH (30 mL) was added and stirred for 24 h. The mixture was then concentrated and recrystallized with $CHCl_3$ and MeOH to afford a white solid 12 (0.677 g, 70%). ^{1}H NMR (400 MHz, CD_3OD): δ = 2.30−2.25 (m, 2H), 1.73−1.32 (m, 20H).

Modification of Phosphonic Acid SAM on ZnO Nanowires. Modification solutions (0.1 mM) were prepared by dissolving a powder of phosphonic acid in THF at room temperature. The annealed ZnO nanowire array was dipped into the solution (5 mL) for 2 h at room temperature. Then, the samples were washed several times with THF.

ALD of Metal Oxides on SAM-Modified and Bare ZnO Nanowires. ALD of metal oxides on SAM-modified and bare ZnO nanowire array was conducted by Veeco Savannah G2. The following five steps are performed to form one ALD cycle. Step 1: evacuate the chamber (about 20 Pa) with 20 sccm N_2 flow. Step 2: supply a given precursor by opening the precursor-supplying valve for T_1 s. Step 3: wait for T_2 s with continuous N_2 flow. Step 4: supply H_2O by opening the precursor-supplying valve for 0.015 s. Step 5: wait for T_3 s with continuous N_2 flow. Each experimental parameter is summarized in Table S3. It should be noted that we selected the lowest possible temperature for each ALD precursor within the range provided by the manufacturer of the ALD equipment used in this study to minimize the thermal decomposition of the SAM skeletons. All the used temperatures (150 or 200 °C) are sufficiently low since the alkyl skeletons are reported to begin decomposing at around 250 °C.[36]

FT-IR Analysis of SAM. The FT-IR spectra of the surface molecules on the ZnO nanowires were recorded at room temperature on a Thermo Fisher Scientific Nicolet iS50 FT-IR spectrometer equipped with a mercury−cadmium−telluride detector. 300 scans were accumulated to obtain each spectrum with a resolution of 4 cm^{-1}. The test room was always purged with dry air. FT-IR spectra for bare ZnO were used as the background spectrum for the other measurements.

In Situ QCM Analysis of Metal Oxide Deposition by ALD. The deposition process of metal oxides was monitored by QCM during the ALD process. Tama device SEN-9E-H-10 was used for sensors. The oscillation frequency of ZnO-nanowire-modified QCM sensors was counted by Tama device THQ-100P-SW and Iwatsu SC-7217A.

STEM Analysis of Nanostructures. STEM images were acquired using JEOL JEM-ARM200F or Thermo Fisher Scientific Titan cubed G2 60-300, which is equipped with a spherical aberration corrector (DCOR, CEOS) for the probe-forming lens system and a Super-X system for EDS. The microscope was operated at an accelerating voltage of 300 kV. The convergence semiangle of the electron probe was set to 18 mrad. The typical probe diameter was less than 0.1 nm. An annular dark-field detector was positioned to detect scattered electrons with an angular range from 38 to 184 mrad.

SEM Analysis of Nanostructures. Scanning electron microscope (SEM) images were acquired using a JEOL JSM-7610F.

■ ASSOCIATED CONTENT

Ⓢ Supporting Information

The Supporting Information is available free of charge at https://pubs.acs.org/doi/10.1021/acsami.3c04470.

> X-ray diffraction analyses for ZnO nanowires on varied substrates, estimation of the thickness of SAM by density functional theory (DFT) calculation, the effect of the density of terminal OH groups of SAMs on TiO_2 deposition, IR pMAIRS analysis of aliphatic phosphonic acid monolayers, a magnified STEM image of ZnO deposited on OH-SAM, mass gain data during ZnO-ALD on OH-SAM-modified and bare ZnO nanowires, IR spectra of OH-SAM before and after ALD and conversion ratios, DFT calculation for the reaction enthalpy (ΔE) through ALD, the effect of bottom metal

oxide layers on CH_3-SAM structures, IR spectra and mass gain data of superlattices, and NMR spectra for identifying (16-hydroxyhexadecyl)phosphonic acid (PDF)

■ AUTHOR INFORMATION

Corresponding Authors

Takuro Hosomi − *Department of Applied Chemistry, Graduate School of Engineering, The University of Tokyo, Tokyo 113-8656, Japan; JST, PRESTO, Kawaguchi, Saitama 332-0012, Japan;* orcid.org/0000-0002-5649-6696; Email: t-hosomi@g.ecc.u-tokyo.ac.jp

Takeshi Yanagida − *Department of Applied Chemistry, Graduate School of Engineering, The University of Tokyo, Tokyo 113-8656, Japan; Institute for Materials Chemistry and Engineering, Kyushu University, Kasuga, Fukuoka 816-8580, Japan;* orcid.org/0000-0003-4837-5701; Email: yanagida@g.ecc.u-tokyo.ac.jp

Authors

Takeshi Ono − *Department of Applied Chemistry, Graduate School of Engineering, The University of Tokyo, Tokyo 113-8656, Japan;* orcid.org/0009-0007-3046-4729

Sae Mitamura − *Department of Applied Chemistry, Graduate School of Engineering, The University of Tokyo, Tokyo 113-8656, Japan*

Hikaru Saito − *Institute for Materials Chemistry and Engineering, Kyushu University, Kasuga, Fukuoka 816-8580, Japan;* orcid.org/0000-0001-9578-1433

Midori Ikeuchi − *Institute for Materials Chemistry and Engineering, Kyushu University, Kasuga, Fukuoka 816-8580, Japan*

Jiangyang Liu − *Department of Applied Chemistry, Graduate School of Engineering, The University of Tokyo, Tokyo 113-8656, Japan;* orcid.org/0000-0001-5456-7705

Kazuki Nagashima − *Department of Applied Chemistry, Graduate School of Engineering, The University of Tokyo, Tokyo 113-8656, Japan; JST, PRESTO, Kawaguchi, Saitama 332-0012, Japan;* orcid.org/0000-0003-0180-816X

Tsunaki Takahashi − *Department of Applied Chemistry, Graduate School of Engineering, The University of Tokyo, Tokyo 113-8656, Japan; JST, PRESTO, Kawaguchi, Saitama 332-0012, Japan;* orcid.org/0000-0002-2840-8038

Wataru Tanaka − *Department of Applied Chemistry, Graduate School of Engineering, The University of Tokyo, Tokyo 113-8656, Japan*

Masaki Kanai − *Department of Applied Chemistry, Graduate School of Engineering, The University of Tokyo, Tokyo 113-8656, Japan*

Complete contact information is available at:
https://pubs.acs.org/10.1021/acsami.3c04470

Notes

The authors declare no competing financial interest.

■ REFERENCES

(1) Karttunen, A. J.; Tynell, T.; Karppinen, M. Atomic-Level Structural and Electronic Properties of Hybrid Inorganic-Organic ZnO:Hydroquinone Superlattices Fabricated by ALD/MLD. *J. Phys. Chem. C* **2015**, *119*, 13105−13114.

(2) Tynell, T.; Yamauchi, H.; Karppinen, M. Hybrid Inorganic-Organic Superlattice Structures with Atomic Layer Deposition/Molecular Layer Deposition. *J. Vac. Sci. Technol., A* **2014**, *32*, 01A105.

(3) Li, M.; Dai, M.; Chabal, Y. J. Atomic Layer Deposition of Aluminum Oxide on Carboxylic Acid-Terminated Self-Assembled Monolayers. *Langmuir* **2009**, *25*, 1911−1914.

(4) Lee, B. H.; Lee, K. H.; Im, S.; Sung, M. M. Monolayer-Precision Fabrication of Mixed-Organic-Inorganic Nanohybrid Superlattices for Flexible Electronic Devices. *Org. Electron.* **2008**, *9*, 1146−1153.

(5) Fang, M.; Kim, C. H.; Martin, B. R.; Mallouk, T. E. Surface Sol-Gel Synthesis of Ultrathin Titanium and Tantalum Oxide Films. *J. Nanopart. Res.* **1999**, *1*, 43−49.

(6) Ichinose, I.; Kawakami, T.; Kunitake, T. Alternate Molecular Layers of Metal Oxides and Hydroxyl Polymers Prepared by the Surface Sol-Gel Process. *Adv. Mater.* **1998**, *10*, 535−539.

(7) Ha, Y.-G.; Emery, J. D.; Bedzyk, M. J.; Usta, H.; Facchetti, A.; Marks, T. J. Solution-Deposited Organic-Inorganic Hybrid Multilayer Gate Dielectrics. Design, Synthesis, Microstructures, and Electrical Properties with Thin-Film Transistors. *J. Am. Chem. Soc.* **2011**, *133*, 10239−10250.

(8) Maehara, Y.; Takenaka, S.; Shimizu, K.; Yoshikawa, M.; Shiratori, S. Buildup of Multilayer Structures of Organic-Inorganic Hybrid Ultra Thin Films by Wet Process. *Thin Solid Films* **2003**, *438−439*, 65−69.

(9) Ito, T.; Okayama, Y.; Shiratori, S. The Fabrication of Organic/inorganic Multilayer by Wet Process and Sequential Adsorption Method. *Thin Solid Films* **2001**, *393*, 138−142.

(10) Johnson, R. W.; Hultqvist, A.; Bent, S. F. A Brief Review of Atomic Layer Deposition: From Fundamentals to Applications. *Mater. Today* **2014**, *17*, 236−246.

(11) George, S. M. Atomic Layer Deposition: An Overview. *Chem. Rev.* **2010**, *110*, 111−131.

(12) Ritala, M.; Leskelä, M.; Dekker, J.-P.; Mutsaers, C.; Soininen, P. J.; Skarp, J. Perfectly Conformal TiN and Al2O3 Films Deposited by Atomic Layer Deposition. *Chem. Vap. Deposition* **1999**, *5*, 7−9.

(13) Avila, J. R.; Emery, J. D.; Pellin, M. J.; Martinson, A. B. F.; Farha, O. K.; Hupp, J. T. Porphyrins as Templates for Site-Selective Atomic Layer Deposition: Vapor Metalation and in Situ Monitoring of Island Growth. *ACS Appl. Mater. Interfaces* **2016**, *8*, 19853−19859.

(14) Canlas, C. P.; Lu, J.; Ray, N. A.; Grosso-Giordano, N. A.; Lee, S.; Elam, J. W.; Winans, R. E.; Van Duyne, R. P.; Stair, P. C.; Notestein, J. M. Shape-Selective Sieving Layers on an Oxide Catalyst Surface. *Nat. Chem.* **2012**, *4*, 1030−1036.

(15) Lee, B. H.; Ryu, M. K.; Choi, S.-Y.; Lee, K.-H.; Im, S.; Sung, M. M. Rapid Vapor-Phase Fabrication of Organic−Inorganic Hybrid Superlattices with Monolayer Precision. *J. Am. Chem. Soc.* **2007**, *129*, 16034−16041.

(16) Sundberg, P.; Karppinen, M. Organic and Inorganic-Organic Thin Film Structures by Molecular Layer Deposition: A Review. *Beilstein J. Nanotechnol.* **2014**, *5*, 1104−1136.

(17) Liu, J.; Yoon, B.; Kuhlmann, E.; Tian, M.; Zhu, J.; George, S. M.; Lee, Y.-C.; Yang, R. Ultralow Thermal Conductivity of Atomic/Molecular Layer-Deposited Hybrid Organic-Inorganic Zincone Thin Films. *Nano Lett.* **2013**, *13*, 5594−5599.

(18) Li, Y.-H.; Wang, D.; Buriak, J. M. Molecular Layer Deposition of Thiol−Ene Multilayers on Semiconductor Surfaces. *Langmuir* **2010**, *26*, 1232−1238.

(19) Meng, X. An Overview of Molecular Layer Deposition for Organic and Organic-Inorganic Hybrid Materials: Mechanisms, Growth Characteristics, and Promising Applications. *J. Mater. Chem. A* **2017**, *5*, 18326−18378.

(20) Patwardhan, S.; Cao, D. H.; Schatz, G. C.; Martinson, A. B. F. Atomic Layer Deposition Nucleation on Isolated Self-Assembled Monolayer Functional Groups: A Combined DFT and Experimental Study. *ACS Appl. Energy Mater.* **2019**, *2*, 4618−4628.

(21) Xu, Y.; Musgrave, C. B. A DFT Study of the Al2O3 Atomic Layer Deposition on SAMs: Effect of SAM Termination. *Chem. Mater.* **2004**, *16*, 646−653.

(22) Borbón-Nuñez, H. A.; Muñiz, J.; El Hachimi, A. G.; Frausto-Silva, D.; Gutiérrez-Díaz, J. L.; Domínguez, D.; Tiznado, H.; Cuentas-Gallegos, A. K. Effect of Oxygen Based Functional Groups on the Nucleation of TiO2 by Atomic Layer Deposition: A Theoretical and Experimental Study. *Mater. Chem. Phys.* **2021**, *267*, 124588.

(23) Dube, A.; Sharma, M.; Ma, P. F.; Ercius, P. A.; Muller, D. A.; Engstrom, J. R. Effects of Interfacial Organic Layers on Nucleation, Growth, and Morphological Evolution in Atomic Layer Thin Film Deposition. *J. Phys. Chem. C* **2007**, *111*, 11045−11058.

(24) Lee, J. P.; Jang, Y. J.; Sung, M. M. Atomic Layer Deposition of TiO2 Thin Films on Mixed Self-Assembled Monolayers Studied as a Function of Surface Free Energy. *Adv. Funct. Mater.* **2003**, *13*, 873−876.

(25) Moshe, H.; Vanbel, M.; Valev, V. K.; Verbiest, T.; Dressler, D.; Mastai, Y. Chiral Thin Films of Metal Oxide. *Chemistry* **2013**, *19*, 10295−10301.

(26) Seo, E. K.; Lee, J. W.; Sung-Suh, H. M.; Sung, M. M. Atomic Layer Deposition of Titanium Oxide on Self-Assembled-Monolayer-Coated Gold. *Chem. Mater.* **2004**, *16*, 1878−1883.

(27) Kobayashi, N. P.; Donley, C. L.; Wang, S.-Y.; Williams, R. S. Atomic Layer Deposition of Aluminum Oxide on Hydrophobic and Hydrophilic Surfaces. *J. Cryst. Growth* **2007**, *299*, 218−222.

(28) Gong, B.; Parsons, G. N. Quantitative in Situ Infrared Analysis of Reactions between Trimethylaluminum and Polymers during Al2O3 Atomic Layer Deposition. *J. Mater. Chem.* **2012**, *22*, 15672.

(29) George, S. M.; Yoon, B.; Dameron, A. A. Surface Chemistry for Molecular Layer Deposition of Organic and Hybrid Organic−Inorganic Polymers. *Acc. Chem. Res.* **2009**, *42*, 498−508.

(30) Orsini, A.; Falconi, C. ZnO Nanowires for Feedback-Assisted Tuning of Electromechanical Resonators. *ACS Appl. Nano Mater.* **2022**, *5*, 15817−15825.

(31) Erol, A.; Okur, S.; Yağmurcukardeş, N.; Arıkan, M. Ç. Humidity-Sensing Properties of a ZnO Nanowire Film as Measured with a QCM. *Sens. Actuators, B* **2011**, *152*, 115−120.

(32) Avila, J. R.; DeMarco, E. J.; Emery, J. D.; Farha, O. K.; Pellin, M. J.; Hupp, J. T.; Martinson, A. B. F. Real-Time Observation of Atomic Layer Deposition Inhibition: Metal Oxide Growth on Self-Assembled Alkanethiols. *ACS Appl. Mater. Interfaces* **2014**, *6*, 11891−11898.

(33) Wilson, C. A.; Grubbs, R. K.; George, S. M. Nucleation and Growth during Al2O3 Atomic Layer Deposition on Polymers. *Chem. Mater.* **2005**, *17*, 5625−5634.

(34) Wang, C.; Hosomi, T.; Nagashima, K.; Takahashi, T.; Zhang, G.; Kanai, M.; Zeng, H.; Mizukami, W.; Shioya, N.; Shimoaka, T.; Tamaoka, T.; Yoshida, H.; Takeda, S.; Yasui, T.; Baba, Y.; Aoki, Y.; Terao, J.; Hasegawa, T.; Yanagida, T. Rational Method of Monitoring Molecular Transformations on Metal-Oxide Nanowire Surfaces. *Nano Lett.* **2019**, *19*, 2443−2449.

(35) Wang, C.; Hosomi, T.; Nagashima, K.; Takahashi, T.; Zhang, G.; Kanai, M.; Yoshida, H.; Yanagida, T. Phosphonic Acid Modified ZnO Nanowire Sensors: Directing Reaction Pathway of Volatile Carbonyl Compounds. *ACS Appl. Mater. Interfaces* **2020**, *12*, 44265−44272.

(36) Yamaguchi, R.; Hosomi, T.; Otani, M.; Nagashima, K.; Takahashi, T.; Zhang, G.; Kanai, M.; Masai, H.; Terao, J.;

Yanagida, T. Maximizing Conversion of Surface Click Reactions for Versatile Molecular Modification on Metal Oxide Nanowires. *Langmuir* **2021**, *37*, 5172−5179.

(37) Pązik, R.; Andersson, R.; Kępiński, L.; Nedelec, J.-M.; Kessler, V. G.; Seisenbaeva, G. A. Surface Functionalization of the Metal Oxide Nanoparticles with Biologically Active Molecules Containing Phosphonate Moieties. Case Study of BaTiO3. *J. Phys. Chem. C* **2011**, *115*, 9850−9860.

(38) Zhang, B.; Kong, T.; Xu, W.; Su, R.; Gao, Y.; Cheng, G. Surface Functionalization of Zinc Oxide by Carboxyalkylphosphonic Acid Self-Assembled Monolayers. *Langmuir* **2010**, *26*, 4514−4522.

(39) Lange, I.; Reiter, S.; Pätzel, M.; Zykov, A.; Nefedov, A.; Hildebrandt, J.; Hecht, S.; Kowarik, S.; Wöll, C.; Heimel, G.; Neher, D. Tuning the Work Function of Polar Zinc Oxide Surfaces Using Modified Phosphonic Acid Self-Assembled Monolayers. *Adv. Funct. Mater.* **2014**, *24*, 7014−7024.

(40) Marcinko, S.; Fadeev, A. Y. Hydrolytic Stability of Organic Monolayers Supported on TiO2 and ZrO2. *Langmuir* **2004**, *20*, 2270−2273.

(41) Thissen, P.; Valtiner, M.; Grundmeier, G. Stability of Phosphonic Acid Self-Assembled Monolayers on Amorphous and Single-Crystalline Aluminum Oxide Surfaces in Aqueous Solution. *Langmuir* **2010**, *26*, 156−164.

(42) Hofer, R.; Textor, M.; Spencer, N. D. Alkyl Phosphate Monolayers, Self-Assembled from Aqueous Solution onto Metal Oxide Surfaces. *Langmuir* **2001**, *17*, 4014−4020.

(43) Hauffman, T.; Blajiev, O.; Snauwaert, J.; van Haesendonck, C.; Hubin, A.; Terryn, H. Study of the Self-Assembling of n-Octylphosphonic Acid Layers on Aluminum Oxide. *Langmuir* **2008**, *24*, 13450−13456.

(44) Bai, S. N.; Tsai, H. H.; Tseng, T. Y. Structural and Optical Properties of Al-Doped ZnO Nanowires Synthesized by Hydrothermal Method. *Thin Solid Films* **2007**, *516*, 155−158.

(45) Muchuweni, E.; Sathiaraj, T. S.; Nyakotyo, H. Effect of Annealing on the Microstructural, Optical and Electrical Properties of ZnO Nanowires by Hydrothermal Synthesis for Transparent Electrode Fabrication. *Mater. Sci. Eng., B* **2018**, *227*, 68−73.

(46) Muchuweni, E.; Sathiaraj, T. S.; Nyakotyo, H. Hydrothermal Synthesis of ZnO Nanowires on Rf Sputtered Ga and Al Co-Doped ZnO Thin Films for Solar Cell Application. *J. Alloys Compd.* **2017**, *721*, 45−54.

(47) Huang, J.; Lee, M.; Lucero, A.; Cheng, L.; Kim, J. Area-Selective ALD of TiO2 Nanolines with Electron-Beam Lithography. *J. Phys. Chem. C* **2014**, *118*, 23306−23312.

(48) Yarbrough, J.; Shearer, A. B.; Bent, S. F. Next Generation Nanopatterning Using Small Molecule Inhibitors for Area-Selective Atomic Layer Deposition. *J. Vac. Sci. Technol., A* **2021**, *39*, 021002.

(49) Groner, M. D.; Fabreguette, F. H.; Elam, J. W.; George, S. M. Low-Temperature Al2O3 Atomic Layer Deposition. *Chem. Mater.* **2004**, *16*, 639−645.

(50) Rocklein, M. N.; George, S. M. Temperature-Induced Apparent Mass Changes Observed during Quartz Crystal Microbalance Measurements of Atomic Layer Deposition. *Anal. Chem.* **2003**, *75*, 4975−4982.

(51) Chen, R.; Kim, H.; McIntyre, P. C.; Bent, S. F. Self-Assembled Monolayer Resist for Atomic Layer Deposition of HfO2 and ZrO2 High-κ Gate Dielectrics. *Appl. Phys. Lett.* **2004**, *84*, 4017−4019.

(52) Hashemi, F. S. M.; Prasittichai, C.; Bent, S. F. A New Resist for Area Selective Atomic and Molecular Layer Deposition on Metal-Dielectric Patterns. *J. Phys. Chem. C* **2014**, *118*, 10957−10962.

(53) Bobb-Semple, D.; Nardi, K. L.; Draeger, N.; Hausmann, D. M.; Bent, S. F. Area-Selective Atomic Layer Deposition Assisted by Self-Assembled Monolayers: A Comparison of Cu, Co, W, and Ru. *Chem. Mater.* **2019**, *31*, 1635−1645.

(54) Nilsen, O.; Mohn, C. E.; Kjekshus, A.; Fjellvåg, H. Analytical Model for Island Growth in Atomic Layer Deposition Using Geometrical Principles. *J. Appl. Phys.* **2007**, *102*, 024906.

(55) Porter, M. D.; Bright, T. B.; Allara, D. L.; Chidsey, C. E. D. Spontaneously Organized Molecular Assemblies. 4. Structural

Characterization of n-Alkyl Thiol Monolayers on Gold by Optical Ellipsometry, Infrared Spectroscopy, and Electrochemistry. *J. Am. Chem. Soc.* **1987**, *109*, 3559−3568.

(56) Spori, D. M.; Venkataraman, N. V.; Tosatti, S. G. P.; Durmaz, F.; Spencer, N. D.; Zürcher, S. Influence of Alkyl Chain Length on Phosphate Self-Assembled Monolayers. *Langmuir* **2007**, *23*, 8053−8060.

(57) Hostetler, M. J.; Stokes, J. J.; Murray, R. W. Infrared Spectroscopy of Three-Dimensional Self-Assembled Monolayers: n-Alkanethiolate Monolayers on Gold Cluster Compounds. *Langmuir* **1996**, *12*, 3604−3612.

(58) Feichtenschlager, B.; Lomoschitz, C. J.; Kickelbick, G. Tuning the Self-Assembled Monolayer Formation on Nanoparticle Surfaces with Different Curvatures: Investigations on Spherical Silica Particles and Plane-Crystal-Shaped Zirconia Particles. *J. Colloid Interface Sci.* **2011**, *360*, 15−25.

(59) Dubey, M.; Weidner, T.; Gamble, L. J.; Castner, D. G. Structure and Order of Phosphonic Acid-Based Self-Assembled Monolayers on Si(100). *Langmuir* **2010**, *26*, 14747−14754.

(60) Sutton, C. C. R.; da Silva, G.; Franks, G. V. Modeling the IR Spectra of Aqueous Metal Carboxylate Complexes: Correlation between Bonding Geometry and Stretching Mode Wavenumber Shifts. *Chemistry* **2015**, *21*, 6801−6805.

(61) Afshar, A.; Cadien, K. C. Growth Mechanism of Atomic Layer Deposition of Zinc Oxide: A Density Functional Theory Approach. *Appl. Phys. Lett.* **2013**, *103*, 251906.

(62) Kosmulski, M. Isoelectric Points and Points of Zero Charge of Metal (Hydr)Oxides: 50years after Parks' Review. *Adv. Colloid Interface Sci.* **2016**, *238*, 1−61.

(63) Zhang, Y.; Ram, M. K.; Stefanakos, E. K.; Goswami, D. Y. Synthesis, Characterization, and Applications of ZnO Nanowires. *J. Nanomater.* **2012**, *2012*, 1−22.

(64) Pulsipher, A.; Westcott, N. P.; Luo, W.; Yousaf, M. N. Rapid in Situ Generation of Two Patterned Chemoselective Surface Chemistries from a Single Hydroxy-Terminated Surface Using Controlled Microfluidic Oxidation. *J. Am. Chem. Soc.* **2009**, *131*, 7626−7632.

(65) Novotný, J.; Pospěchová, K.; Hrabálek, A.; Čáp, R.; Vávrová, K. Synthesis of Fluorescent C24-Ceramide: Evidence for Acyl Chain Length Dependent Differences in Penetration of Exogenous NBD-ceramides into Human Skin. *Bioorg. Med. Chem. Lett.* **2009**, *19*, 6975−6977.

(66) Pawsey, S.; McCormick, M.; De Paul, S.; Graf, R.; Lee, Y. S.; Reven, L.; Spiess, H. W. ^{1}H Fast MAS NMR Studies of Hydrogen-Bonding Interactions in Self-Assembled Monolayers. *J. Am. Chem. Soc.* **2003**, *125*, 4174−4184.